RSC Advances

PAPER

View Article Online
View Journal | View Issue

Cite this: RSC Adv., 2018, 8, 24049

Effect of cationic disorder on the energy generation and energy storage applications of $Ni_xCo_{3-x}S_4$ thiospinel†

Charles Gervas,[a] Malik Dilshad Khan,[a] Chunyang Zhang,[b] Chen Zhao,[b] Ram K. Gupta,[b] Emanuela Carleschi,[c] Bryan P. Doyle[c] and Neerish Revaprasadu*[a]

Received 24th April 2018
Accepted 27th June 2018

DOI: 10.1039/c8ra03522a

rsc.li/rsc-advances

Thiospinels show interesting catalytic and energy storage applications, however, the cationic disorder can have major influence on the energy generation and/or energy storage applications. In this study, the effect of stoichiometric variation of metals in a thiospinel *i.e.* $Ni_xCo_{3-x}S_4$, is examined on energy generation and storage properties. Nickel- or cobalt-rich $Ni_xCo_{3-x}S_4$ nanosheets were prepared by the hot injection method using single molecular precursors. The nanosheets were characterized by p-XRD, TEM, HR-TEM, EDX and XPS techniques. Nickel-rich and cobalt-rich nanosheets were tested for oxygen and hydrogen evolution reactions and for supercapacitance performance. It was observed that the nickel-rich $Ni_xCo_{3-x}S_4$ nanosheets have superior energy storage and energy generation properties.

Introduction

Various electroactive materials such as transition metal sulfides (*e.g.* NiS_x, CuS_x, and CoS_x),[1,2] carbonaceous materials,[3] oxides of transition metals[4] and conducting polymers[5] are regarded as good materials for supercapacitors. However, the cycling performance of transition metal sulfides is not satisfactory as they pulverize electrode materials in the course of cycling, which leads to poor electrical connectivity to electrode materials from current collectors. Similarly, the low capacitance of carbon-based materials, average electronic conductivity for oxides of transition metals, high cost *e.g.* $RuO_x \cdot nH_2O$ and poor cyclic stability of conducting polymers make supercapacitors, fabricated from these materials, less efficient.[6]

Recently oxide and sulfide based ternary compounds of cobalt and nickel have attracted the attention of researchers due to their high efficiency in energy generation and energy storage devices. Ternary metallic oxides, such as $NiCo_2O_4$, have been considered appropriate for the fabrication of supercapacitors, being a better-conducting material than the binary oxides of the parent metals *i.e.* nickel and cobalt.[7–9] However, $NiCo_2O_4$ shows less electron conductivity when compared to its sulfide counterpart, $NiCo_2S_4$. Furthermore, the Ni–Co–S system provides the material with improved performance and stability as compared to the oxide counterpart and their binary counterparts, Co–S and Ni–S.[10–12]

Thiospinels are sulfur based ternary compounds that exist in the spinel structure, whose general formula is AB_2S_4 (where $A = M^{2+}$ and $B = M^{3+}$). Such a structure is said to be built on a closely packed array of S^{-2} ions, with A^{2+} and B^{3+} metallic ions occupying the tetrahedral and octahedral sites respectively.[13] This means the ternary Ni–Co(S) system such as $NiCo_2S_4$ with a normal spinel structure has the synergetic effect from both Ni^{2+} and Co^{3+} in the presence of S^{2-}, hence making the material better for both electrochemical activities as well as electrocatalytic activities for H_2 and O_2 evolution reactions.

Ternary Ni–Co(S) system has superior quality electrocatalytic activities for oxygen and hydrogen evolution studies.[14,15] The bimetallic catalysts of Fe, Ni, Co with the chalcogen atom (S, Se, Te) are potentially efficient candidates because of their natural abundance (hence low cost),[16] and high electrocatalytic activity, especially when attached to smaller organic molecules.[17] Bimetallic chalcogenides fit in better than binary sulfides due to synergetic effects of the transition metal atoms that often exhibit collective higher catalytic activity in different chemical environments.

Various protocols have been used to fabricate $NiCo_2S_4$. They include hydrothermal methods,[16] electrochemical depositions,[18] anion exchange methods,[19] controlled sulfurization methods,[20] and chemical bath deposition.[21] The hydrothermal method is the predominant protocol used in the preparation of $NiCo_2S_4$ as it is considered to be cost-effective and environment friendly as compared to other protocols. Lou and co-workers synthesized hollow nanofibers, ball-in-ball hollow spheres,

---

[a] Department of Chemistry, University of Zululand, Private Bag X1001, Kwa-Dlangezwa 3880, South Africa. E-mail: RevaprasaduN@unizulu.ac.za

[b] Department of Chemistry, Pittsburg State University, Pittsburg, Kansas, USA

[c] Department of Physics, University of Johannesburg, P. O. Box 524, Auckland Park, 2006, Johannesburg, South Africa

† Electronic supplementary information (ESI) available: TGA, p-XRD and EDX, electrochemical plots and Tables. See DOI: 10.1039/c8ra03522a

and onion-like $NiCo_2S_4$ particles *via* the ion-exchange method.[22–24] The controlled growth of $NiCo_2S_4$ nanosheets on a graphene matrix was shown to lead to superior supercapacitive performance.[9] Peng *et al.* reported the hydrothermal synthesis of a $NiCo_2S_4$-RGO hybrid and investigated its electrochemical performance.[25]

In ternary and/or quaternary semiconductors, stoichiometric variations play an important role and this composition tunability is the key property to their characteristics and device performance.[26] Non-stoichiometric compounds are not really desirable as, in II–V or III–V compounds, it results in low-performing device characteristics. However, for ternary materials, this is not necessarily always true. It was observed for Cu/(Ag)InS_2 nanomaterials that the In-rich compounds are better emitters as compared to Ag- or Cu-rich compositions.[27] Similarly, a slight cationic disorder in $AgBiS_2$ results in a significant change in electronic properties.[28] Although, there are some examples of cationic disorders of I–III–V compounds, the effect of cationic disorder on energy storage and/or energy generation performance of thiospinels is not very well explored.

The use of single molecular precursors is often known to give superior results in nanomaterials synthesis as it makes use of preformed bonds with the decomposition product easily predicted.[29–33] Furthermore, they are equally suitable for the synthesis of nanomaterials and deposition of thin films.[34–38]

Herein, we have designed a facile one-pot synthesis of $Ni_xCo_{3-x}S_4$ thiospinel using dithiocarbamate complexes of nickel and cobalt as single molecular precursors by thermolyzing the stoichiometric amounts of the complexes in a hot primary amine. This protocol has enabled us to tune the morphology and stoichiometry of $Ni_xCo_{3-x}S_4$. It was observed that the nanoparticles synthesized at 200 °C were cobalt-rich, whereas the higher temperature (250 °C) results in the nickel-rich material. The effect of stoichiometric disorder of metals, on the energy storage and energy generation properties, has been examined in detail.

Experimental

Materials

Ethyl piperazine 99%, carbon disulfide 99%, nickel acetate (Sigma Aldrich), cobalt chloride hexahydrate (Sigma Aldrich), oleylamine (OLA) 99%, sodium hydroxide (99%), methanol (99.5%), chloroform, acetone, and hexane were used as purchased without any further purification.

Synthesis of ligand and metal (Co, Ni) complexes

Ethyl piperazine dithiocarbamate ligand and the corresponding nickel/cobalt complexes were synthesized using the procedures described elsewhere.[39] The synthesis of complexes is detailed as follows: nickel acetate (2.35 g, 9.43 mmol) was dissolved in the deionized water (25.0 mL), and then added drop-wise to the solution of the dithiocarbamate ligand (4.0 g, 18.86 mmol). Whereas, the cobalt complex was prepared by dissolving (2.25 g, 9.43 mmol) of cobalt chloride hexahydrate in deionized water (25.0 mL), followed by the drop-wise addition to the aqueous solution of ligand *i.e.* (4.0 g, 18.86 mmol). The reaction mixtures were stirred for 45 min, and the precipitates formed were vacuum filtered, washed with deionized water and dried in an oven at 80 °C overnight. The complexes formed were analyzed by the CHN and FT-IR analysis: [Ni(Etpz-dtc)$_2$] (**1**), (where Etpz-dtc = ethylpiperazinyl dithiocarbamato) yield: 81%. Microanalysis: calculated for $C_{14}H_{26}N_4NiS_4$: C, 38.45; H, 5.99; N, 12.81. Found: C, 38.36; H, 6.01; N, 12.93. IR (cm^{-1}, ATR): 1006.93, ν (C=S); 1431, ν (C=N); 1499.69, ν (C–N); 452–360, ν (Ni–S). [Co(Etpz-dtc)$_3$] (**2**), (where Etpz = ethylpiperazinyl and dtc = dithiocarbamato) yield: 91%. Microanalysis: calculated for $C_{21}H_{39}CoN_6S_6$: C, 40.23; H, 6.27; N, 13.41. Found: C, 40.11; H, 6.08; N, 13.62. IR (cm^{-1}, ATR): 1012.45, ν (C=S); 1455, ν (C=N); 1522.61, ν (C–N).

Synthesis of $NiCo_2S_4$ nanosheets

In a typical procedure, stoichiometric amounts of nickel and cobalt complexes (1 : 1) were dissolved in 3.0 mL of OLA as a dispersing/coordinating solvent and injected into preheated OLA (5.0 mL) in a three-necked flask at 200 °C. A temperature drop of about 15 °C was observed and the solution immediately turned black. The reaction temperature was maintained for 2 hours, after which the heating was stopped. A 30.0 mL mixture of methanol and acetone (v/v 1 : 1) was used for precipitation of OLA capped $Ni_xCo_{3-x}S_4$ nanoparticles, which were then washed and separated by centrifugation. The reaction was also carried out at a higher temperature of 250 °C under similar conditions.

Characterization

Microanalysis was performed on a Perkin-Elmer automated model 2400 series II CHNS/O analyzer. Infrared spectra were recorded on a Bruker FT-IR Tensor 27 spectrophotometer directly on small samples of the compounds in the 200–4000 cm^{-1} range. Thermogravimetric analysis was carried out at a heating rate of 10 °C min^{-1}, using a Perkin Elmer Pyris 6 TGA up to 600 °C in a closed perforated aluminium pan under N_2 gas flow. TEM and HRTEM analyses were performed using a JEOL 1010 TEM and JEOL 2100 HRTEM. Samples were prepared by placing a drop of a dilute solution of nanoparticles on formvar-coated Cu grids (150 mesh) for TEM and holey carbon grids for HRTEM. The samples were allowed to dry completely at room temperature and viewed at an accelerating voltage of 100 kV (TEM) and 200 kV (HRTEM). The images were captured digitally using a Megaview III camera; stored and measured using Soft Imaging Systems iTEM software (TEM) and Gatan camera and Gatan software (HRTEM). Powder X-ray diffraction (p-XRD) patterns were recorded in the high angle 2θ range of 20–80° using a Bruker AXS D8 Advance X-ray diffractometer, equipped with nickel-filtered CuKα radiation ($\lambda = 1.5406$ Å) at 40 kV, 40 mA at room temperature. X-ray photoemission spectroscopy (XPS) measurements were acquired at room temperature by means of a SPECS PHOIBOS 150 electron energy analyzer, using a Al K_α monochromatized photon source ($h\nu = 1486.71$ eV). The overall (photon + analyser) energy resolution was set to 0.8 eV for survey spectra and to 0.6 eV for all the high-resolution XPS spectra shown here.

Electrochemical studies

Electrochemical characterizations of the samples were performed using the three-electrode system. Working electrodes were prepared by coating mixture of $Ni_xCo_{3-x}S_4$ (80 wt%), acetylene black (10 wt%), and polyvinylidene difluoride (10 wt%) in *N*-methyl pyrrolidinone (NMP) on to a nickel foam. A platinum wire and saturated calomel electrode were used as a counter and a reference electrode in 3 M KOH as an electrolyte. A supercapacitor device was fabricated using two working electrodes separated by ion transporting layer. The size of the device was 0.25 cm^2. Before assembling the device, both working electrodes and ion-transporting layer were soaked in the 3 M KOH for 1 h. Versa STAT 4-500 electrochemical workstation (Princeton Applied Research, USA) was used to perform cyclic voltammetry, galvanostatic charge–discharge, and electrochemical impedance spectroscopy (EIS) measurements. EIS measurements were carried out by applying an AC voltage with 10 mV amplitude in a frequency range from 0.05 Hz to 10 kHz at open circuit potential.

The electrocatalytic behavior of the $Ni_xCo_{3-x}S_4$ samples for oxygen evolution reaction (OER) and hydrogen evolution reaction (HER) was also examined using standard three electrode system consisting of $NiCo_2S_4$ on nickel foam as a working electrode, platinum wire as a counter electrode and saturated calomel electrode (SCE) as a reference in 1 M KOH electrolyte. Electrocatalytic testing includes linear sweep voltammetry (LSV), cyclic voltammetry (CV), chronoamperometry and electrochemical impedance spectroscopy. LSV was performed at a scan rate of 2 mV s^{-1} in both OER and HER region. The potential was converted to RHE using the Nernst equation. All the EIS measurements were recorded in a frequency range of 0.05 Hz to 10 kHz with an applied 10 mV of AC amplitude.

Results and discussions

The complexes were prepared by simple metathetical reactions. It was observed that, although, cobalt(II)chloride was used for the synthesis of cobalt complex, however, the *in situ* oxidation of cobalt yields the complex with cobalt in +3 oxidation state. Similar behavior of *in situ* oxidation of cobalt from +2 to +3 state has been observed before and is well reported.[40]

The thermal stability of the complexes was observed by thermogravimetric analysis (TGA) and is shown in Fig. S1 (ESI†). Complex (**1**) decomposes in two steps, where a major mass loss of about (72%) was observed at 324 °C, followed by a minor weight loss of about (7.3%) around 385 °C, suggesting the progressive loss of the sulfur atoms. Complex (**2**) shows single step decomposition with a weight loss of 79.16% at 289 °C. The residue obtained from the complex (**1**) (21.09%) and complex (**2**) (20.84%) was found to be very close to the calculated values for NiS (20.75%) and CoS (20.82%) respectively.

Both complexes show high thermal stability, however, $Ni_xCo_{3-x}S_4$ nanoparticles were synthesized with ease in OLA, at a temperature quite lower than the decomposition temperature as determined by TGA. The use of oleylamine (OLA) has two major advantages; the long alkyl chain helps in the effective capping of the nanoparticles,[41] and the primary amine can catalyze the breakdown of the molecular precursors, initiating decomposition at low temperature.[42] Both nickel and cobalt sulfides can exist in spinel structures *i.e.* Co_3S_4 and Ni_3S_4. Similarly, a combination of both in different ratios can also be used for generation of thiospinel lattice, such as $NiCo_2S_4$, $CoNi_2S_4$ and $(Ni, Co)_3S_4$. Most of the work has been done on energy applications of $NiCo_2S_4$ but little on nickel incorporated Co_3S_4 (*i.e.* $Ni_xCo_{3-x}S_4$).

The complexes [Ni(Etpzdtc)$_2$] and [Co(Etpzdtc)$_3$], were dispersed in OLA in stoichiometric amounts (1 : 1), and injected in OLA at 200 °C and/or 250 °C, under similar reaction conditions. The effect of temperature was examined on the morphology, crystallinity, and composition of the synthesized $Ni_xCo_{3-x}S_4$ nanoparticles. The phase of the synthesized OLA capped $Ni_xCo_{3-x}S_4$ nanoparticles, was determined by p-XRD measurements (ESI Fig. S2†). The diffraction peaks can be indexed to the (220), (311), (400), (422), (511), (440), (533), (444) and (553) which matches well with the standard pattern (ICDD # 01-073-1704). The diffraction peaks are respectively positioned at $2\theta = 26.84°, 31.58°, 38.32°, 47.40°, 50.47°, 55.31°, 65.10°, 69.29°, 78.76°$. There is no detectable impurity, secondary phase or unassigned peaks. The intensity of the peaks was comparatively weaker at a lower temperature (200 °C) and more pronounced at a higher temperature of 250 °C. Coordinating solvents can reduce the decomposition temperature of both precursors, however, crystallinity can only be enhanced by increasing the temperature. The absence of binary phases, such as NiO, CoO, NiS, and CoS confirms the phase purity of nanomaterials prepared from single molecular precursors. The p-XRD displays typical behavior of cobalt-rich minerals *i.e.* the rising trend of the diffraction pattern from the baseline. It is due to the fact that the energy of the Kα radiation of copper is higher than the k-absorption edge of cobalt, hence, cobalt fluoresce strongly and give rise to such behaviour. The calculation of the lattice constant using diffraction peak (311) resulted in 9.319 Å which is in agreement with previous reports.[21]

The microscopic analysis of the morphology of the nanomaterials, synthesized at both temperatures, is shown in Fig. 1. The synthesis of $Ni_xCo_{3-x}S_4$ at a temperature of 200 °C, indicates the formation of nanosheets. The sheets were stacked and showed a poly-dispersed nature whereas, the size of the nanosheets, was in the order of microns. The crystalline nature of the nanosheets was indicated by clear lattice fringes and the presence of well-defined spots in the SAED pattern (Fig. 1(b)). Similar sheet-like morphology was observed for $Ni_xCo_{3-x}S_4$ synthesized at a higher temperature of 250 °C (Fig. 1(c)). However, the rate of nucleation increases many folds with an increase of temperature, hence, growth defects such as twinning and some stacking faults were also observed by TEM analysis (Fig. 1(d)).

Fig. 1(e) shows high-angle annular dark-field (HAADF) image and the elemental mapping indicates a uniform distribution of all elements in the sample. The composition by ICP analysis indicates that the sample prepared at 200 °C was cobalt-rich and the exact composition of the sample was found to be

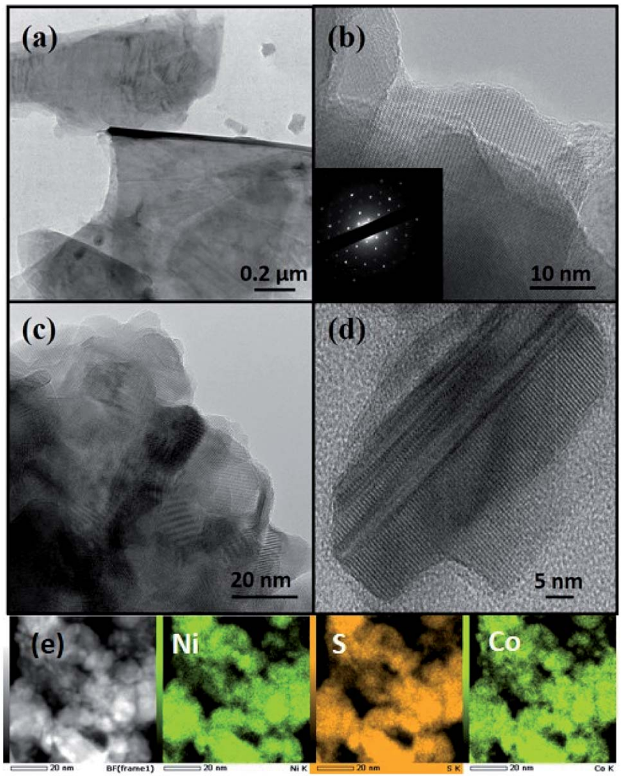

Fig. 1 TEM images for OLA capped $Ni_xCo_{3-x}S_4$ synthesized at (a and b) 200 °C (c and d) 250 °C and (e) shows HAADF image along with elemental mapping of nanosheets synthesized at 200 °C.

$Ni_{1.22}Co_{1.50}S_{4.31}$ (henceforth referred to as NiCoS-1), whereas, the sample synthesized at 250 °C was nickel-rich, and a stoichiometric composition of $Ni_{1.63}Co_{1.18}S_{4.17}$ (henceforth referred to as NiCoS-2) was observed.

XPS analysis

XPS measurements were performed in order to investigate the electronic structure and the oxidation states of Ni, Co, and S in both samples of the $Ni_xCo_{3-x}S_4$ series. Fig. 2(a) shows the comparison of the wide scans for the investigated samples. Spectra show all expected peaks, as well as O, C, and N. O may be derived from the exposure of the sample to the atmosphere, whereas C and N (present in very moderate quantities) derive from the use of oleylamine.

Fig. 2(c) shows the Co 2p core level for the investigated samples. The Co 2p binding energy region is dominated by two sharp peaks located at ~779 eV and ~794 eV binding energy, and two broad peaks at ~780.5 eV and ~796.5 eV, which correspond to the Co $2p_{3/2}$ and Co $2p_{1/2}$ spin–orbit components for Co^{3+} and Co^{2+} oxidation states, respectively. The identification of Co^{2+} and Co^{3+} oxidation states is consistent with what is published in the literature for similar NiCo-based systems.[43–45] Together with the main peaks, two weak shake-up satellites are detected at about 6.5 eV towards higher binding energy from the Co^{3+} peaks. The line shape of this core level has been fitted using three spin–orbit doublets, as shown in Fig. 2(c). Each doublet is separated by a spin–orbit splitting of approximately 15.1 eV. The overall fit to the experimental data (thick line) shows good agreement with the raw data. Table S1 (ESI†) displays the Co $2p_{3/2}$ binding energy of the three doublets, as well as the area ratio between Co^{2+}/Co^{3+} oxidation states. As one can see, the area changes quite drastically from one sample to the other, reflecting an intrinsic difference in the electronic structure within the series.

Fig. 2(d) shows the comparison of the fitted Ni 2p XPS core level spectra. The Ni $2p_{3/2}$ and $2p_{1/2}$ spectral regions are composed of three spin–orbit doublets corresponding to (in order from lower to higher binding energy) Ni^{3+}, Ni^{2+} oxidation states and a broad shake-up satellite of the Ni^{3+} species, respectively. As for the Co 2p core level above, the fitted components (together with a Shirley-type background) appear in Fig. 2(d) together with the raw data. Table S2† (ESI†) displays the Ni $2p_{3/2}$ binding energy of the three doublets, as well as the area ratio between Ni^{2+}/Ni^{3+} oxidation states. Interestingly, the ratios for Ni oxidation states have an opposite trend with respect to those for Co. This was to be expected as charge neutrality of the samples has to be ensured.

In general, the line shapes of the Co 2p and Ni 2p core levels reported here and the observation that both ions are present in divalent and trivalent oxidation states are consistent with previous studies for $NiCo_2S_4$.[18,45] The elements nickel, cobalt, and sulfur have the tendency to exist in two mineralogical forms *i.e.* $NiCo_2S_4$ or $CoNi_2S_4$. In $NiCo_2S_4$, Ni is in the +2 oxidation state, whereas Co is in the +3 oxidation state. However, a small amount of Ni can convert to +3 oxidation state and Co can occupy the site with +2 oxidation state. The ratio can be increased if, comparatively, one of the element is in slight excess, and can occupy the position of the deficient element as well to stabilize the spinel framework.

The XPS results from the S 2p core level are reported in Fig. 2(b). The line shape is consistent with previous reports on these systems.[44,45] Because the spin–orbit splitting between the $2p_{3/2}$ and the $2p_{1/2}$ peaks in sulfur is only 1.18 eV (*i.e.* of the same order of magnitude as the experimental resolution for these measurements), we have decided to report the $2p_{3/2}$ and the $2p_{1/2}$ peaks as separate peaks in the figure. This is to aid in visualization of the fits to the spectra. The main spin–orbit doublet at lower binding energy is attributed to S in the 2- oxidation state. This is typically what happens when sulfur ions bond with metallic ions in ternary metal sulfides.[46] The S 2p doublets whose $2p_{3/2}$ peaks are observed at 164 eV and 169 eV are attributed to surface sulfur with high oxide state, such as sulfites and sulfates, respectively. The binding energies of the $2p_{3/2}$ core level for these three doublets are reported in Table S3† (ESI†).

Energy generation application

The OER performance of the NiCoS-1 and NiCoS-2 was first investigated. Fig. 3(a) shows the LSV polarization curves for $Ni_xCo_{3-x}S4$ samples in 1 M KOH. It can be observed that the NiCoS-2 exhibited the lower overpotential of 327 mV to generate a current density of 10 mA cm^{-2}, while NiCoS-1 needs overpotential of 348 mV at 10 mA cm^{-2}. The OER kinetics of the

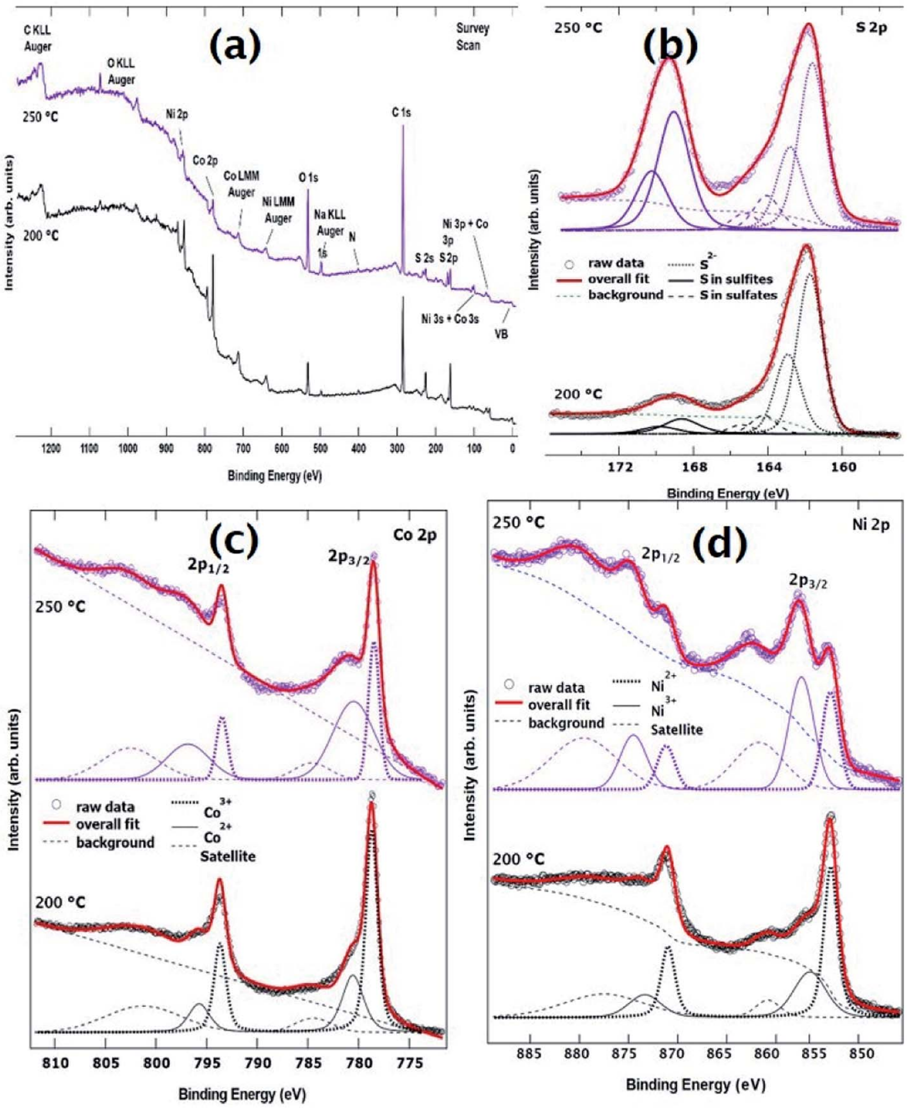

Fig. 2 (a) XPS survey spectra (b) S 2p core level spectra (c) Co 2p core level spectra and (d) Ni 2p core level spectra for both samples synthesized at 200 °C and 250 °C.

electrocatalysts were further analyzed using Tafel plots. As seen in Fig. 3(b), the Tafel slope for the NiCoS-1 and NiCoS-2 was calculated to be 90 and 89 mV dec^{-1} respectively. The lower Tafel slope for NiCoS-2 indicated faster OER catalytic kinetics than NiCoS-1. The lower overpotential and faster kinetics suggest that NiCoS-2 has a better electrocatalytic performance compared to NiCoS-1. One of the reasons for that could be the nickel-richness of the sample synthesized at 250 °C. As shown by the XPS analysis that the concentration of the Ni^{3+} was higher in NiCoS-2 sample, and the high activity of material, in the presence of mixed valence states can be explained by a self-doping phenomenon of the material.[47] The increase in Ni^{3+} species may result in n-type doping as it provide extra electrons, whereas Co^{2+} may lead to p-type doping by providing extra holes. Hence, a higher Ni^{3+} concentration will result in enhanced electrical conductivity for electrons, therefore leads to better electrochemical performance.[48] In addition, high-temperature synthesis of the NiCoS-2 yielded higher crystallinity compared to NiCoS-1, resulted in the enhanced electrocatalytic performance.[49] From the overall observation, both NiCoS-1 and NiCoS-2 have a better or comparable performance than other reported $NiCo_2S_4$ samples. Liu *et al.* have synthesized $NiCo_2S_4$ nanowires array through sulfidization of the $NiCo_2S_4$ precursor which was uniformly grown on the carbon cloth using a hydrothermal reaction.[50] The synthesized $NiCo_2S_4$ electrocatalyst required an overpotential of 340 mV to generate a current density of 100 mA cm^{-2} with a Tafel slope of 89 mV dec^{-1}. $NiCo_2S_4$ with porous nanosheets array topology on carbon cloth was prepared by Zhu *et al.* through two-step hydrothermal process showed a Tafel slope of 91 mV dec^{-1}.[51] Table S4 (ESI†) shows the comparison with other recently reported OER catalyst using non-precious metals in the alkaline medium.

The HER activity of the $Ni_xCo_{3-x}S_4$ samples was also studied, the polarization curves for $Ni_xCo_{3-x}S_4$ samples in HER region is given in Fig. 3(c). As seen in Fig. 3(c), NiCoS-2 required an

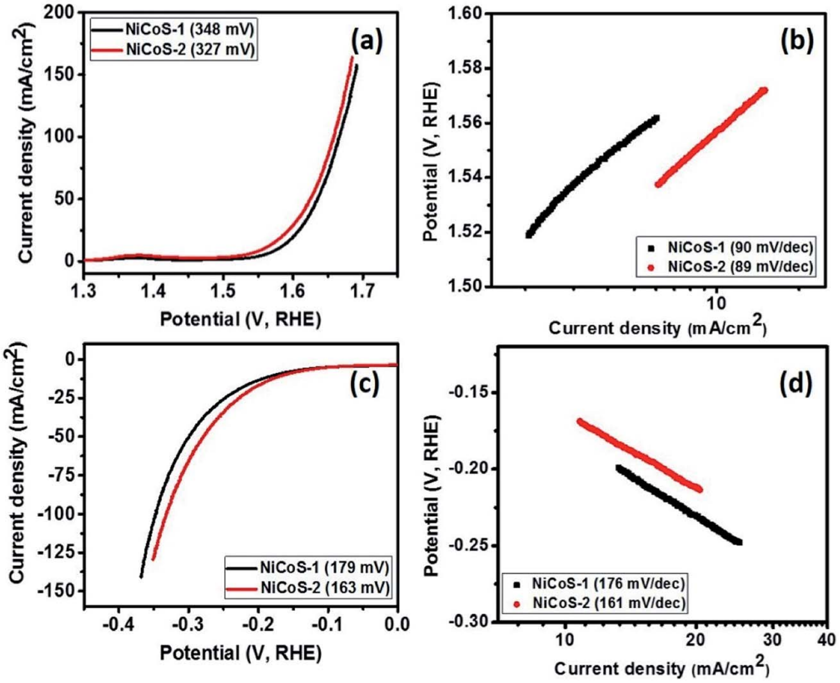

Fig. 3 (a) Polarization curves and (b) Tafel slopes for Ni$_x$Co$_{3-x}$S$_4$ samples in OER range and (c) polarization curves and (d) Tafel slopes for Ni$_x$Co$_{3-x}$S$_4$ samples in HER range.

overpotential 163 mV, while NiCoS-1 required an overpotential of 179 mV to achieve a current density of 10 mA cm^{-2}. As seen in the polarization curves, NiCoS-2 showed significant improvement in the HER performance compared to NiCoS-1. It can be observed from Fig. 3(d), the Tafel slope for NiCoS-1 and NiCoS-2 was calculated to be 176 and 161 mV dec^{-1}, respectively. The lower Tafel slope for NiCoS-2 showed faster HER kinetics for electrocatalysts, which confirmed the better HER performance. Sivanantham *et al.* have used a two-step hydrothermal method to complete the *in situ* growth of hierarchical NiCo$_2$S$_4$ nanowire arrays on a nickel foam substrate, which needed an overpotential of 210 mV to deliver a hydrogen production current density of 10 mA cm^{-2}.[52] The NiCo$_2$S$_4$ electrocatalyst prepared by Liu *et al.* required an overpotential of 305 mV to generate a current density of 10 mA cm^{-2} with a Tafel slope of 141 mV dec^{-1}.[50] The NiCo$_2$S$_4$ with porous nanosheets array topology showed an overpotential of 181 mV to reach 10 mA cm^{-2}.[51] The other recently reported HER catalytic properties using Ni, Co, and other non-precious metals in the alkaline medium are given in Table S5 (ESI†).

To further understand the reason for improved electrocatalytic properties of NiCoS-2 sample, the electrochemical active surface area of NiCoS-1 and NiCoS-2 was determined using cyclic voltammograms in the non-faradic region. All the CV measurements were performed in a potential range of 0.87–0.92 V (*vs.* RHE), where no faradic reactions were observed. The CV curves were recorded for NiCoS-1 and NiCoS-2 at various scan rates to determine the electrochemical double layer capacitance (C_{dl}), which is directly proportional to the electrochemical active surface area of the sample. C_{dl} was calculated by plotting half of the difference in positive and negative current densities at 0.895 V (*vs.* RHE) *versus* the scan rates (Fig. 4(a)). The C_{dl} value of the NiCoS-1 and NiCoS-2 was calculated to be 2.27 and 7.48 mC cm^{-2}, respectively. The effective

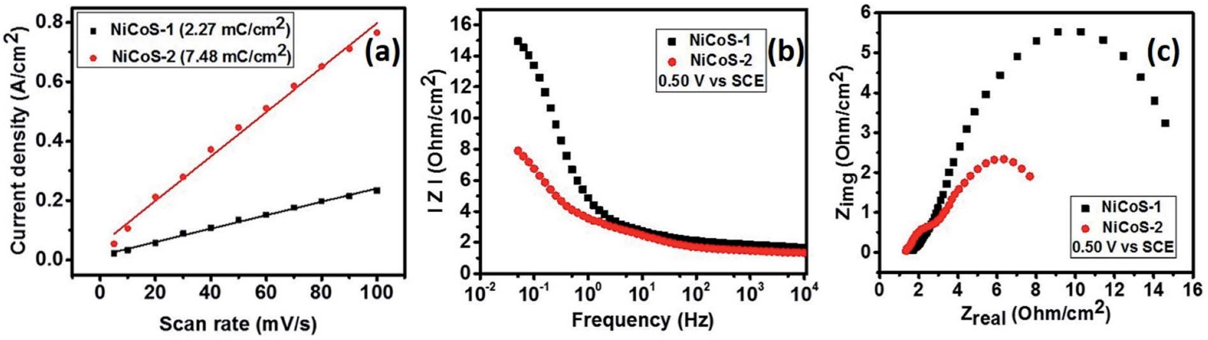

Fig. 4 (a) Current density *vs.* scan rate plots for Ni$_x$Co$_{3-x}$S$_4$ samples, (b) $|Z|$ *vs.* frequency plots and (c) Z_{real} *vs.* Z_{img} plots for NiCo$_2$S$_4$ samples at 0.5 V (*vs.* SCE).

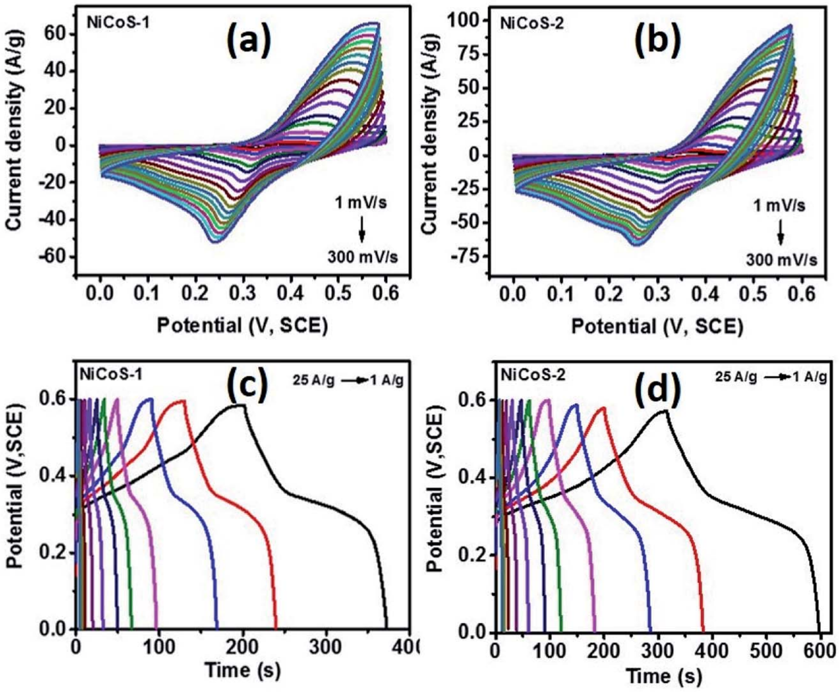

Fig. 5 CV curves of (a) NiCoS-1 and (b) NiCoS-2 at various scan rates in 3 M KOH electrolyte. Galvanostatic charge–discharge curves of (c) NiCoS-1 and (d) NiCoS-2 at various scan rates in 3 M KOH electrolyte.

electrochemical surface area of the NiCoS-2 is more than 3 times higher than that of the NiCoS-1. The highest active electrochemical surface area provides NiCoS-2 the better OER and HER activity than NiCoS-1.[53]

The electrocatalytic properties of $Ni_xCo_{3-x}S_4$ samples were further analyzed using electrochemical impedance spectroscopy tests. From Fig. 4(b), which is the plots of total impedance $|Z|$ *versus* frequency, it is observed that NiCoS-2 has the lower total impedance, having only about half of the impedance of NiCoS-1. Moreover, NiCoS-2 has smaller semicircle in the Nyquist plots (Fig. 4(c)). The smaller radius of the semicircle at low-frequency region suggests a lower charge

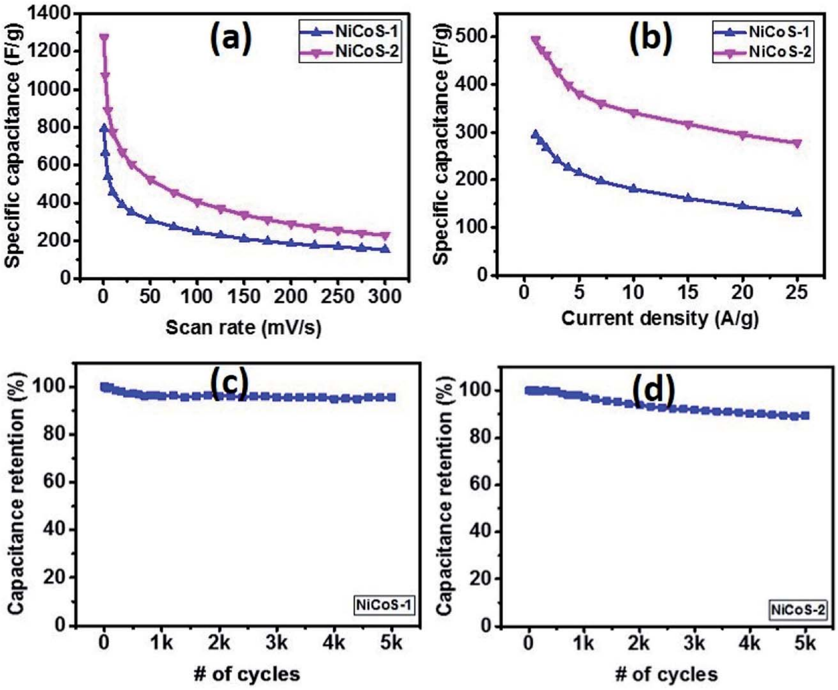

Fig. 6 Variation of specific capacitance as a function of (a) scan rate and (b) current density for $Ni_xCo_{3-x}S_4$ samples. Cyclic stability plot for (c) NiCoS-1 and (d) NiCoS-2 sample using galvanostatic charge–discharge measurements.

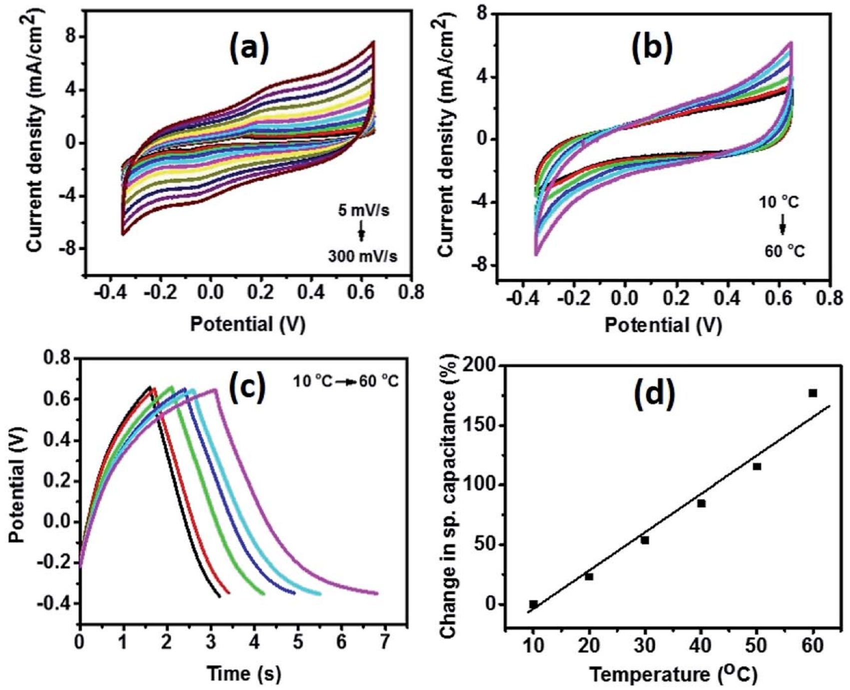

Fig. 7 CV curves (a) at various scan rates and (b) at various temperature, (c) charge–discharge curves at various temperature and (d) change in specific capacitance as a function of temperature for the supercapacitor device fabricated using NiCoS-2 electrodes.

transfer resistance and a faster electron transfer during electrochemical reactions. Therefore, the results of EIS tests show that the NiCoS-2 possesses an excellent electrocatalytic performance which is consistent with the excellent OER and HER performance.

The total impedance $|Z|$ and Nyquist plots of NiCoS-2 at various potentials are shown in Fig. S3 (ESI†). It is observed that the total impedance $|Z|$ decreases with increasing potential, indicating improved electrocatalytic performance at higher potential. Similarly, the Nyquist plot starts to convert to semicircle from a straight line with the increase in the potential (Fig. S4(b)†). That is because semicircle region depends on overpotential as the increase in potential provides faster reaction which leads to the reduction of semicircle's diameter.

The electrocatalytic long-term durability was measured using chronoamperometry. It was observed that the current density of NiCoS-2 was maintained almost at a constant level of 10 mA cm^{-2} over the 16 h duration (Fig. S4, ESI†). The little negative effect on current density with increasing time confirms that the NiCoS-2 is very stable and could be used as a durable electrocatalyst for water splitting applications.

Energy storage application

The supercapacitor performance of $Ni_xCo_{3-x}S_4$ samples was evaluated using cyclic voltammetry and galvanostatic charge–discharge (GCD) tests. Fig. 5(a) and (b) show the CV curves of NiCoS-1 and NiCoS-2 in a 3 M KOH solution at various scan rates in the voltage range of 0–0.6 V (*vs.* SCE). The presence of redox peaks revealed the occurrence of faradaic redox reactions in both CV curves of $Ni_xCo_{3-x}S_4$ samples. The peak potentials for oxidation reaction and reduction reaction are about 0.45 V and 0.25 V, bilateral shifting with the increase of scan rate. In addition, the larger current density of redox peaks and area under the CV curves for NiCoS-2 indicate the higher charge storage capacity. Moreover, from GCD curves of both $Ni_xCo_{3-x}S_4$ samples (Fig. 5(c) and (d)), under the same current density, NiCoS-2 have the longer charge and discharge time compared to NiCoS-1, further suggesting the superior charge storage capacity. The nonlinear lines charge and discharge curves showed the pseudo-capacitance behaviour attributed to reversible redox reactions at the electrode surface.

Specific capacitance of NiCoS-1 and NiCoS-2 were calculated from the CV data and GCD data and was plotted in Fig. 6(a) and (b) as a function of scan rates and current densities, respectively. Higher specific capacitance was observed at a lower scan rate and lower current density for both $Ni_xCo_{3-x}S_4$ samples because of lower scan rate and lower current density provides more time for redox reactions. The maximum specific capacitance of NiCoS-2 was 1273 F g^{-1} and 494 F g^{-1} which were calculated from the CV curve at a scan rate of 1 mV s^{-1} and GCD curve at 1 A g^{-1}, respectively. The supercapacitor performances of NiCoS-1 and NiCoS-2 are superior or comparable to other reported NiCo-based samples. The $NiCo_2O_4$ coral-like porous crystals synthesized using sol–gel approach by Wu *et al.* have a capacitance of 217 F g^{-1}.[54] Salunkhe *et al.* prepared $NiCo_2O_4$ films on indium tin oxide substrates by a chemical bath deposition method. The $NiCo_2O_4$ films showed a highest specific capacitance of 490 F g^{-1}.[55]

The long-term performance of the $Ni_xCo_{3-x}S_4$ samples was studied using galvanostatic charge–discharge measurements for 5000 cycles (Fig. 6(c and d)). As seen in the capacitance *versus* number of cycles, both samples exhibited a very stable performance. The NiCoS-1 and NiCoS-2 showed a capacitance retention of 95% and 85% after 5000 cycles, respectively. About 60% of capacitance was maintained after 1000 cycles for the ultrathin porous hierarchically textured $NiCo_2O_4$–graphene oxide nanosheets.[9] The capacitance of caterpillar-like $NiCo_2S_4$ nanocrystal arrays on nickel foam prepared by Chen *et al.* kept 83% after 3000 cycles.[56]

To further evaluate the performance of NiCoS-2 as energy storage material and the effect of temperature on the electrochemical properties, a symmetrical supercapacitor device was fabricated and tested in 3 M KOH using CV, GCD, and EIS. Fig. 7(a) shows the CV curves of the device at various scan rates. The potential window was as large as 1 V. From the CV curves of the device at various temperatures (Fig. 7(b)), the area under the CV curves was observed to increase with increasing temperature, showing improvement in storage capacity of the device. Similar behavior was observed in the GCD curves at different temperatures (Fig. 7(c)). Charge and discharge time increased with temperature confirming the improvement in charge storage capacity. As seen in Fig. 7(d), there was a 180% increase in specific capacitance when the temperature was raised from 10 to 60 °C. The total impedance $|Z|$ with different frequency and Nyquist plots at various temperatures are given in (ESI Fig. S5(a) and (b)†). As seen, total impedance $|Z|$, Z_{real} and Z_{imag} decreases with increasing temperature, which could be due to increased mobility of the ions in the electrolyte.[47] Similar phenomena was observed in other reports.[8,57] A 150% improvement in the specific capacitance of the device using flower-structure $NiCo_2O_4$ by increasing temperature from 10 to 60 °C.[8]

Conclusions

In summary, Co or Ni enriched nanosheets of $Ni_xCo_{3-x}S_4$ were synthesized using piperazino–dithiocarbamate complexes of cobalt and nickel as single source precursors. The nanosheets were used for oxygen evolution reaction and a lower Tafel slope (89 mV dec^{-1}) was observed for Ni-rich nanosheets which indicates better OER performance, as compared to Co-rich nanosheets (90 mV dec^{-1}). Similarly, the Tafel slope for Co-rich and Ni-rich were calculated to be 176 and 161 mV dec^{-1} respectively, which shows the superior HER performance of Ni-rich nanosheets. The efficiency of $Ni_xCo_{3-x}S_4$ nanosheets was also investigated for supercapacitance performance. The GCD curves indicate superior charge storage performance of Ni-rich nanosheets and a maximum specific capacitance of 1273 F g^{-1} and 494 F g^{-1} were observed from the CV curve at a scan rate of 1 mV s^{-1} and GCD curve at 1 A g^{-1}. Both samples exhibited a very stable long-term performance and Co-rich *versus* Ni-rich samples showed a capacitance retention of 95% and 85% after 5000 cycles, respectively. Overall, the Ni-rich $Ni_xCo_{3-x}S_4$ sample indicates a superior energy generating and storage efficiency. The study indicates the significance of the metallic stoichiometric variation on properties of thiospinel materials, and a way to tune the efficiency of the ternary materials by the slight modification of metallic composition.

Conflicts of interest

Authors declare no conflict of interest.

Acknowledgements

The authors are grateful to the National Research Foundation (NRF) South African Research Chairs Initiative (SARChI) for financial support. Dr Ram K. Gupta expresses his sincere acknowledgment to the Polymer Chemistry Program and Kansas Polymer Research Center, Pittsburg State University for providing financial and research support. We acknowledge JEOL, UK for the high resolution electron microscopy images. Part of the equipment used in this study was funded through NRF grant 93205.

Notes and references

1 H. Zhang, X. Yu, D. Guo, B. Qu, M. Zhang, Q. Li and T. Wang, *ACS Appl. Mater. Interfaces*, 2013, **5**, 7335–7340.
2 H. Wan, X. Ji, J. Jiang, J. Yu, L. Miao, L. Zhang, S. Bie, H. Chen and Y. Ruan, *J. Power Sources*, 2013, **243**, 396–402.
3 L. Hao, X. Li and L. Zhi, *Adv. Mater.*, 2013, **25**, 3899–3904.
4 Y. Zhang, L. Li, H. Su, W. Huang and X. Dong, *J. Mater. Chem. A*, 2015, **3**, 43–59.
5 Q. Wu, Y. Xu, Z. Yao, A. Liu and G. Shi, *ACS Nano*, 2010, **4**, 1963–1970.
6 C.-C. Hu and W.-C. Chen, *Electrochim. Acta*, 2004, **49**, 3469–3477.
7 Y. Zhu, X. Ji, Z. Wu, W. Song, H. Hou, Z. Wu, X. He, Q. Chen and C. E. Banks, *J. Power Sources*, 2014, **267**, 888–900.
8 R. K. Gupta, J. Candler, S. Palchoudhury, K. Ramasamy and B. K. Gupta, *Sci. Rep.*, 2015, **5**, 15265.
9 E. Mitchell, A. Jimenez, R. K. Gupta, B. K. Gupta, K. Ramasamy, M. Shahabuddin and S. R. Mishra, *New J. Chem.*, 2015, **39**, 2181–2187.
10 Y. Zhu, Z. Wu, M. Jing, W. Song, H. Hou, X. Yang, Q. Chen and X. Ji, *Electrochim. Acta*, 2014, **149**, 144–151.
11 L. Niu, Y. Wang, F. Ruan, C. Shen, S. Shan, M. Xu, Z. Sun, C. Li, X. Liu and Y. Gong, *J. Mater. Chem. A*, 2016, **4**, 5669–5677.
12 Z. Yang, X. Zhu, K. Wang, G. Ma, H. Cheng and F. Xu, *Appl. Surf. Sci.*, 2015, **347**, 690–695.
13 C. Biagioni and M. Pasero, *Am. Mineral.*, 2014, **99**, 1254–1264.
14 M. R. Gao, J. Jiang and S. H. Yu, *Small*, 2012, **8**, 13–27.
15 C. Xia, P. Li, A. N. Gandi, U. Schwingenschlögl and H. N. Alshareef, *Chem. Mater.*, 2015, **27**, 6482–6485.
16 S. Y. Khoo, J. Miao, H. B. Yang, Z. He, K. C. Leong, B. Liu and T. T. Y. Tan, *Adv. Mater. Interfaces*, 2015, **2**.
17 J. Liu, J. Wang, B. Zhang, Y. Ruan, L. Lv, X. Ji, K. Xu, L. Miao and J. Jiang, *ACS Appl. Mater. Interfaces*, 2017, **9**, 15364–15372.
18 J. Xiao, L. Wan, S. Yang, F. Xiao and S. Wang, *Nano Lett.*, 2014, **14**, 831–838.
19 C. Xia and H. N. Alshareef, *Chem. Mater.*, 2015, **27**, 4661–4668.

20 F. Lu, M. Zhou, W. Li, Q. Weng, C. Li, Y. Xue, X. Jiang, X. Zeng, Y. Bando and D. Golberg, *Nano Energy*, 2016, **26**, 313–323.
21 D.-Y. Kim, G. Ghodake, N. Maile, A. Kadam, D. S. Lee, V. Fulari and S. Shinde, *Sci. Rep.*, 2017, **7**, 9764.
22 Y. M. Chen, Z. Li and X. W. D. Lou, *Angew. Chem.*, 2015, **127**, 10667–10670.
23 L. Shen, L. Yu, H. B. Wu, X.-Y. Yu, X. Zhang and X. W. D. Lou, *Nat. Commun.*, 2015, **6**, 6694.
24 B. Y. Guan, L. Yu, X. Wang, S. Song and X. W. D. Lou, *Adv. Mater.*, 2017, **29**, 1605051.
25 S. Peng, L. Li, C. Li, H. Tan, R. Cai, H. Yu, S. Mhaisalkar, M. Srinivasan, S. Ramakrishna and Q. Yan, *Chem. Commun.*, 2013, **49**, 10178–10180.
26 P. Rudolph, *Cryst. Res. Technol.*, 2003, **38**, 542–554.
27 B. Chen, H. Zhong, W. Zhang, Z. a. Tan, Y. Li, C. Yu, T. Zhai, Y. Bando, S. Yang and B. Zou, *Adv. Funct. Mater.*, 2012, **22**, 2081–2088.
28 F. Viñes, G. Konstantatos and F. Illas, *Phys. Chem. Chem. Phys.*, 2017, **19**, 27940–27944.
29 L. D. Nyamen, V. R. Pullabhotla, A. A. Nejo, P. T. Ndifon, J. H. Warner and N. Revaprasadu, *Dalton Trans.*, 2012, **41**, 8297–8302.
30 N. Moloto, N. Revaprasadu, M. Moloto, P. O'Brien and M. Helliwell, *Polyhedron*, 2007, **26**, 3947–3955.
31 P. S. Nair, T. Radhakrishnan, N. Revaprasadu, G. Kolawole and P. O'Brien, *J. Mater. Chem.*, 2004, **14**, 581–584.
32 M. D. Khan, J. Akhtar, M. A. Malik and N. Revaprasadu, *ChemistrySelect*, 2016, **1**, 5982–5989.
33 M. D. Khan, M. Akhtar, M. A. Malik, N. Revaprasadu and P. O'Brien, *ChemistrySelect*, 2018, **3**, 2943–2950.
34 M. Khan, M. Malik, J. Akhtar, S. Mlowe and N. Revaprasadu, *Thin Solid Films*, 2017, **638**, 338–344.
35 A. A. Memon, M. Dilshad, N. Revaprasadu, M. A. Malik, J. Raftery and J. Akhtar, *Turk. J. Chem.*, 2015, **39**, 169–178.
36 S. Mlowe, D. J. Lewis, M. A. Malik, J. Raftery, E. B. Mubofu, P. O'Brien and N. Revaprasadu, *New J. Chem.*, 2014, **38**, 6073–6080.
37 M. D. Khan, M. Aamir, M. Sohail, M. Sher, J. Akhtar, M. A. Malik and N. Revaprasadu, *J. Sol. Energy*, 2018, **169**, 526–534.
38 M. D. Khan, M. Aamir, M. Sohail, M. Sher, N. Baig, J. Akhtar, M. A. Malik and N. Revaprasadu, *Dalton Trans.*, 2018, **47**, 5465–5473.
39 C. Gervas, S. Mlowe, M. P. Akerman and N. Revaprasadu, *New J. Chem.*, 2018, **42**(8), 6203.
40 D. P. Dutta, G. Sharma and I. Gopalakrishnan, *Mater. Lett.*, 2008, **62**, 1275–1278.
41 N. Mntungwa, M. Khan, S. Mlowe and N. Revaprasadu, *Mater. Lett.*, 2015, **145**, 239–242.
42 M. D. Khan, J. Akhtar, M. A. Malik, M. Akhtar and N. Revaprasadu, *New J. Chem.*, 2015, **39**, 9569–9574.
43 M. Prabu, K. Ketpang and S. Shanmugam, *Nanoscale*, 2014, **6**, 3173–3181.
44 W. Du, Z. Wang, Z. Zhu, S. Hu, X. Zhu, Y. Shi, H. Pang and X. Qian, *J. Mater. Chem. A*, 2014, **2**, 9613–9619.
45 N. Kurra, C. Xia, M. N. Hedhili and H. N. Alshareef, *Chem. Commun.*, 2015, **51**, 10494–10497.
46 Y. Ohno, *Phys. Rev. B*, 1991, **44**, 1281.
47 X. Li, Q. Li, Y. Wu, M. Rui and H. Zeng, *ACS Appl. Mater. Interfaces*, 2015, **7**, 19316–19323.
48 X. Wang, C. Yan, A. Sumboja, J. Yan and P. S. Lee, *Adv. Energy Mater.*, 2014, **4**, 1301240.
49 S. A. Pervez, D. Kim, U. Farooq, A. Yaqub, J.-H. Choi, Y.-J. Lee and C.-H. Doh, *ACS Appl. Mater. Interfaces*, 2014, **6**, 11219–11224.
50 D. Liu, Q. Lu, Y. Luo, X. Sun and A. M. Asiri, *Nanoscale*, 2015, **7**, 15122–15126.
51 W. Zhu, M. Ren, N. Hu, W. Zhang, Z. Luo, R. Wang, J. Wang, L. Huang, Y. Suo and J. Wang, *ACS Sustainable Chem. Eng.*, 2018, **6**(3), 2893.
52 A. Sivanantham, P. Ganesan and S. Shanmugam, *Adv. Funct. Mater.*, 2016, **26**, 4661–4672.
53 C. Ranaweera, C. Zhang, S. Bhoyate, P. Kahol, M. Ghimire, S. Mishra, F. Perez, B. K. Gupta and R. K. Gupta, *Mater. Chem. Front.*, 2017, **1**, 1580–1584.
54 Y. Q. Wu, X. Y. Chen, P. T. Ji and Q. Q. Zhou, *Electrochim. Acta*, 2011, **56**, 7517–7522.
55 R. R. Salunkhe, K. Jang, H. Yu, S. Yu, T. Ganesh, S.-H. Han and H. Ahn, *J. Alloys Compd.*, 2011, **509**, 6677–6682.
56 X. Chen, D. Chen, X. Guo, R. Wang and H. Zhang, *ACS Appl. Mater. Interfaces*, 2017, **9**, 18774–18781.
57 S. Bhoyate, C. K. Ranaweera, C. Zhang, T. Morey, M. Hyatt, P. K. Kahol, M. Ghimire, S. R. Mishra and R. K. Gupta, *Global Environ.*, 2017, **1**, 1700063.